Catalysis Science & Technology

ROYAL SOCIETY OF CHEMISTRY

PAPER

View Article Online
View Journal

Published on 08 February 2021. Downloaded by NANJING UNIVERSITY on 3/21/2021 12:48:35 PM.

Check for updates

Cite this: DOI: 10.1039/d0cy02298e

# Effects of different treatment atmospheres on $CeO_2$/g-$C_3N_4$ photocatalytic $CO_2$ reduction: good or bad?†

Yu Pu,[a] Wanqin Li,[a] Yandi Cai,[a] Xiaoqian Wei,[a] Xin Wang,[a] Chong Chen,[ab] Weixin Zou*[ab] and Lin Dong *[ab]

Received 29th November 2020,
Accepted 8th February 2021

DOI: 10.1039/d0cy02298e

rsc.li/catalysis

Atmospheric treatment of a photocatalyst is of great significance to the activity. In this work, oxidizing, inert and reducing atmospheres were employed to treat $CeO_2$/g-$C_3N_4$ photocatalysts, denoted as CeCN, CeCN-$N_2$, and CeCN-$H_2$. Interestingly, after $N_2$ treatment, CeCN-$N_2$ showed the best photoreduction $CO_2$ performance, while the poorest activity was observed on CeCN-$H_2$. The obvious reversal of activities was explored. The $H_2$ treatment with stronger reducibility resulted in too many defects, and then bulk defects led to the charge recombination and poor $CO_2$ activation. On the other hand, moderately inert $N_2$ treatment introduced both the surface oxygen defects of $CeO_2$ and amino groups in CN heterocycles, which synergistically enhanced the photoinduced electron–hole separating efficiency and medium base sites for the $CO_2$ activation. Furthermore, a Z-scheme photocatalytic system instead of type II (CeCN) was formed on CeCN-$N_2$, which was provided with stronger redox, and the generated overpotential was beneficial for $CO_2$ photoreduction.

## 1. Introduction

Carbon dioxide ($CO_2$), as the final product of carbon and carbide oxidation, is a major contributor to global warming, which results in serious impacts on the world's ecosystems. As a result, a significant increase in $CO_2$ has become a public environmental concern.[1–3] On this basis, exploring the efficient utilization of $CO_2$ has been taken into consideration by a large number of researchers. Inspired by photosynthesis, solar energy has been used as a green power source to develop clean and efficient $CO_2$ photoreduction.[4,5]

Graphitic carbon nitride (g-$C_3N_4$) is a potential photocatalyst with a narrow band gap and high stability[6] and it has been widely applied to photocatalytic VOCs degradation, water splitting, and $CO_2$ photoreduction.[6–8] However, bulk g-$C_3N_4$ has a high rate of photoelectron–hole recombination as well as few exposed active and adsorption sites.[9] To improve the activity of the g-$C_3N_4$ photocatalyst, several strategies have been used such as doping with other elements or compounding with other semiconductors.[10–12] Heat treatment under different atmospheres is also an effective method to promote electron–hole separation. Wang[13] fabricated $N_2$–g-$C_3N_4$ by heating urea under a nitrogen atmosphere. They reported that the formation of carbon vacancies was a result of heating in the $N_2$ atmosphere. Majima *et al.*[14] developed $C_3N_4$-T-$CO_2$ photocatalysts through a one-step process by the direct pyrolysis treatment of 3-amino-1,2,4-triazole in $CO_2$ atmosphere with no additives. They concluded that the improvement of the $C_3N_4$-T-$CO_2$ photocatalytic activity was ascribed to the formation of $NH_x$ sites, which could generate hydrogen-bonding interactions between $C_3N_4$ layers and the generation of nitrogen vacancies with no charge transport ability under $CO_2$ calcination atmosphere. Dong *et al.*[15] introduced nitrogen defects into the framework of g-$C_3N_4$ by heating g-$C_3N_4$ powder in a hydrogen atmosphere. The $NO^+$ reaction intermediate was formed on nitrogen defects sites and enabled an accelerated photocatalytic reaction, which contributed to the enhanced photocatalytic NO removal.

Ceria ($CeO_2$), as a rare earth element of the lanthanide series, shows attractive prospects in industrial applications due to its abundant oxygen defects, admirable redox ability, and low cost.[16–18] For photocatalysis, oxygen vacancies on the surface of $CeO_2$ can enhance its light absorption ability.[19] Besides, $CeO_2$ is a basic metal oxide, which can not only improve the $CO_2$ adsorption capacity but also transform inert linear $CO_2$ to b-$HCO_3^-$ and then b-$CO_3^{2-}$ lowers the reductive

[a] Key Laboratory of Mesoscopic Chemistry of MOE, School of Chemistry and Chemical Engineering, School of the Environmental, Nanjing University, Nanjing 210093, PR China. E-mail: wxzou2016@nju.edu.cn, donglin@nju.edu.cn
[b] Jiangsu Key Laboratory of Vehicle Emissions Control, Center of Modern Analysis, Nanjing University, Nanjing 210093, PR China

† Electronic supplementary information (ESI) available. See DOI: 10.1039/d0cy02298e

Published on 08 February 2021. Downloaded by NANJING UNIVERSITY on 3/21/2021 12:48:35 PM.

potential of $CO_2$.[20] In addition, $CeO_2$ is often used as a cocatalyst in photocatalysis. Lv *et al.*[19] designed and synthesized $CeO_2$ nanocube-decorated ZIS microspheres for the $CO_2$ photoreduction. It was found that the separation efficiency of the photoelectron and hole of ZIS was significantly promoted by the introduction of $CeO_2$ as a cocatalyst.

Recently, great progress has been made in the research of $CeO_2$/g-$C_3N_4$ composite catalysts. Guo *et al.*[21] designed hollow structured g-$C_3N_4$@$CeO_2$ with rich oxygen vacancies, facilitating photoelectron–hole separation, thus exhibiting higher photocatalytic activity compared with the synthesized pristine g-$C_3N_4$ and $CeO_2$. Huang *et al.*[22] synthesized $CeO_2$/g-$C_3N_4$ for photocatalytic $H_2$ evolution, revealing that the interfacial effect is a critical factor for the enhancement of the photocatalytic activity. Wang *et al.*[23] anchored 0D $CeO_2$ nanocrystals on the 2D layered $MoS_2$/g-$C_3N_4$ nanosheets and the $H_2$ evolution activity was impressively boosted due to the improved visible light adsorption, faster charge separation, and more surface-reactive sites. Wang *et al.*[24] reported a facile method for the synthesis of the $CeO_2$/g-$C_3N_4$ hybrid with enhanced $CO_2$ reduction and ciprofloxacin degradation performance using surface carboxylated g-$C_3N_4$ as the substrate. A built-in electric field was formed at the $CeO_2$/g-$C_3N_4$ heterojunction, which can greatly improve the charge separation and transfer efficiency.

Moreover, heat treatment under different atmospheres could regulate the concentration of oxygen vacancies on $CeO_2$.[25] Qi *et al.*[26] prepared different morphological $CeO_2$ supported Au catalysts with pretreatment under air and $H_2$ atmospheres. They showed a dependence of the catalytic activity on the oxygen vacancy concentration of the catalysts, revealing the correlation between its defect features and the pretreatment atmosphere. In our previous work, the $Cu_2O$/$CeO_2$ catalyst was calcined under a nitrogen atmosphere, which also leads to more oxygen vacancies on the surface of $CeO_2$.[27] Therefore, atmospheric treatment plays an important role in the photocatalytic performance.

Herein, we prepared $CeO_2$/g-$C_3N_4$ catalysts with heat treatment under air, nitrogen, and hydrogen atmospheres. CeCN-$N_2$ shows the highest $CO_2$ photoreduction efficiency, while CeCN-$H_2$ presents poorer $CO_2$ photoreduction activity. The differences in the activities *via* atmospheric treatment were investigated by EPR, PL, XPS, and $CO_2$-TPD characterizations. It was found that the atmospheric treatment has a great influence on the oxygen defects, photogenerated charge transfer, and interfacial electron densities of $CeO_2$ and g-$C_3N_4$. The built-in electronic field and Z-scheme photocatalytic system were formed on CeCN-$N_2$, while type II system was formed on the CeCN photocatalyst, which affected the reducibility of $CO_2$ photoreduction. Furthermore, *in situ* DRIFTS under $CO_2$ and light irradiation was carried out and the reaction mechanism of $CO_2$ photoreduction was proposed. This work would provide a basic guidance for designing efficient Z-scheme catalysts through the atmospheric treatment method.

# 2. Experimental

## 2.1. Catalyst preparation

$CeO_2$ was obtained through cerium nitrate hexahydrate calcination in air at 550 °C for 4 h. The g-$C_3N_4$ support was prepared by heating urea at 550 °C for 4 h in a muffle furnace. Then, the mixture of 5 wt% $CeO_2$ and 95 wt% g-$C_3N_4$ was ultrasonicated for 0.5 h and stirred in a fume hood at 80 °C overnight to remove water. The obtained solids were calcined at 450 °C under air, nitrogen, and hydrogen atmosphere and these $CeO_2$/g-$C_3N_4$ catalysts were denoted as CeCN, CeCN-$N_2$, and CeCN-$H_2$, respectively. The g-$C_3N_4$ support was denoted as CN.

## 2.2. Catalyst characterization

The crystal structures of the catalysts were determined by X-ray diffraction (XRD) on a Philips X'Pert Pro diffractometer under Ni-filtered Cu Kα radiation ($\lambda$ = 0.15418 nm). X-ray photoelectron spectroscopy (XPS, ESCA PHI500) was used to examine the surface chemical composition. The charging effect on the sample was compensated by binding energies referenced to 284.6 eV of the C 1s peak. The attenuated total reflectance-Fourier transform infrared (ATR-FTIR) spectra were collected on a Nicolet IS10 FT-IR spectrometer equipped with an ATR accessory in the range from 400 to 4000 $cm^{-1}$. The background was collected first and then subtracted for every sample. The number of scans was 32 at a resolution of 4 $cm^{-1}$. UV-vis diffuse reflectance spectroscopy (UV-vis DRS) was carried out in the range of 200 to 700 nm with the reference of $BaSO_4$ by a Shimadzu UV-2401 spectrophotometer. The electron paramagnetic resonance (EPR) signals were examined at 110 K on JEOL JESFA200 EPR spectrometers. Thermogravimetry and differential thermal analysis (TG-DTA) of the samples were tested on a Netzsch thermo-analyzer STA 449C from room temperature to 700 °C in air at the rate of 10 mL $min^{-1}$. The trail gas would be introduced to a mass spectrometer if necessary. Raman spectra were obtained on a LABRAM-HR Confocal Laser with a He–Cd laser (325 nm) excitation source. Photoluminescence (PL) spectra were recorded on an F-7000 fluorescence spectrophotometer (Hitachi, Tokyo, Japan). The wavelength of the excitation light was 325 nm. The experiments were carried out in the solid state. The slit in all the measurements was 1.5 nm. $CO_2$-TPD experiments were carried out on a multifunction chemisorption analyzer (Tianjin Pengxiang, China) with a quartz U-tube reactor and detected by a TCD. Each sample (50 mg) was heated under ultra-high purity $N_2$ flow (30 mL $min^{-1}$) up to 100 °C at 10 °C $min^{-1}$ for 30 min and then cooled to room temperature. After pretreatment, $CO_2$ flow (30 mL $min^{-1}$) was passed through the catalyst bed for 30 min; subsequently, the sample was flushed by $N_2$ flow (30 mL $min^{-1}$) for 30 min. Then, TPD analysis was performed under $N_2$ flow (30 mL $min^{-1}$) by heating the sample at the rate of 10 °C $min^{-1}$ up to 550 °C. *In situ* diffuse infrared Fourier transform (*in situ* DRIFT) spectra were recorded under illumination after 30 min $CO_2$


This journal is © The Royal Society of Chemistry 2021

Published on 08 February 2021. Downloaded by NANJING UNIVERSITY on 3/21/2021 12:48:35 PM.

adsorption using a Nicolet iS50 FT-IR spectrometer (Thermo, USA).

Electrochemical measurements including photocurrents, Mott–Schottky (M–S) curves, and electrochemical impedance spectroscopy (EIS) were carried out on a V01344 electrochemical workstation (Tianjin Brillante Technology Limited) with a standard three-electrode cell in 0.5 M $Na_2SO_4$. The photocatalysts were coated onto indium tin oxide (ITO, 1 × 2 $cm^2$) as the working electrodes, while the Ag/AgCl and Pt wires served as the reference electrode and counter electrode, respectively. A 300 W Xe lamp was utilized as the light source.

### 2.3. Catalytic performances measurement

$CO_2$ photoreduction was carried out under 300 W Xe lamp irradiation, which was the only heat throughout the whole experiment, in a 50 mL Teflon-lined autoclave. The photocatalyst (50 mg) was dispersed in 5 mL water and high purity $CO_2$ was added up to 4 bar. The suspension was stirred for 30 min and then irradiated for 8 h with a full spectrum light. The generated products were measured by a gas chromatograph.

The active species produced during photocatalysis swere trapped by adding 0.05 mM benzoquinone for superoxide radicals ($^{\bullet}O_2^-$). The photocatalytic performance of the $CeO_2$/g-$C_3N_4$ samples was explored by the decolorization of methylene blue (MB) (20 mg $L^{-1}$, 80 mL) under 300 W Xe light irradiation with 5 mg of the synthesized samples after stirring for 30 min in the dark. Then, the photocatalytic activity was tested at the maximum absorption wavelength of the UV-vis spectrum of MB with a UV-vis spectrophotometer at room temperature.

## 3. Results and discussion

### 3.1. Catalyst structure

The morphologies of CeCN, CeCN-$N_2$, and CeCN-$H_2$ photocatalysts were investigated by TEM. As shown in Fig. S1,† $CeO_2$ nanoparticles were dispersed onto the 2D-layered $C_3N_4$, showing a close contact between them, and different pretreatment atmospheres had no influence on the morphologies of the $CeO_2$/g-$C_3N_4$ photocatalysts. In addition, the phase structures of the photocatalysts were determined by XRD. The XRD patterns of CeCN, CeCN-$N_2$, CeCN-$H_2$, $CeO_2$, and g-$C_3N_4$ samples are shown in Fig. 1a. CeCN, CeCN-$N_2$, and CeCN-$H_2$ samples show similar diffraction peaks. The peaks appearing at 13.1° and 27.3° are attributed to the (100) and (002) planes of g-$C_3N_4$, respectively.[28] The peaks at 28.7°, 33.3°, 47.8°, and 56.8° are the characteristic peaks of $CeO_2$ (111), (200), (220), and (311) crystal planes, respectively (JCPDS no: 04-0802). Compared to g-$C_3N_4$, the diffraction peak at 27.3° of the CeCN, CeCN-$N_2$, and CeCN-$H_2$ samples showed a slight shift to a higher angle, suggesting a narrowing of the interlayer distance according to the Bragg equation ($2d \sin\theta = n\lambda$)[29] and the presence of interfacial effect between $CeO_2$ and g-$C_3N_4$.

Moreover, TG-DTA was carried out to identify the weight percentage of $CeO_2$ and g-$C_3N_4$. In Fig. S2,† there were no obvious weight changes in the CeCN, CeCN-$N_2$, and CeCN-$H_2$ samples, demonstrating that these photocatalysts present a similar composition. On the basis of the TEM, XRD, and TG-DTA results, it is proposed that pretreatment by different atmospheres, the morphologies, phase structures, and composites were similar on the three CeCN, CeCN-$N_2$, and CeCN-$H_2$ samples, *i.e.*, the morphologies and phase structures of the $CeO_2$/g-$C_3N_4$ photocatalysts were not influenced by the pretreatment atmospheres.

### 3.2. Photocatalytic performance

$CO_2$ photocatalytic reduction was carried out under light illumination with a full spectrum and the presence of water vapor. The photocatalytic performances of $CO_2$ reduction on $CeO_2$/g-$C_3N_4$ nanocomposites pretreated with different atmospheres are exhibited in Fig. 2. After 8 h illumination, CO product was detected on the three photocatalysts, in which CeCN-$N_2$ shows the best catalytic performance, which is approximately 3.5 μmol $h^{-1}$ $g^{-1}$, followed by CeCN, and CeCN-$H_2$ provides the poorest activity. In short, the activity sequence is CeCN-$N_2$ > CeCN > CeCN-$H_2$, suggesting that compared with the CeCN sample, $N_2$ atmosphere treatment is beneficial for $CO_2$ photoreduction, while $H_2$ atmosphere treatment is not conducive. In order to explore the different and opposite effects of atmosphere treatment on the photocatalytic performances, the properties of photo-generated charge transfer and reactant $CO_2$ activation of CeCN, CeCN-$N_2$, and CeCN-$H_2$ were determined in detail.

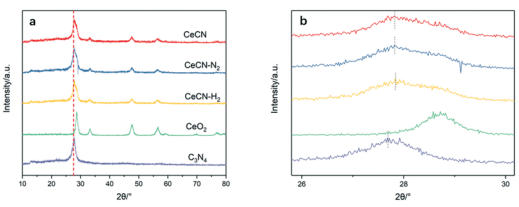


Fig. 1 (a) XRD patterns and (b) enlarged XRD patterns of the $CeO_2$/g-$C_3N_4$ samples.

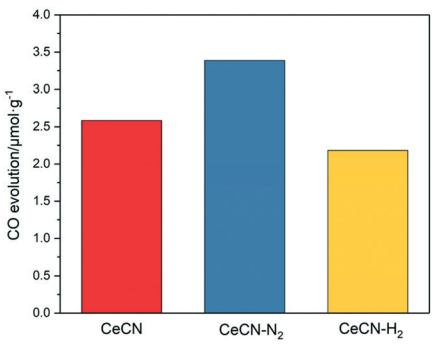


Fig. 2 $CO_2$ photoreduction activities of the $CeO_2$/g-$C_3N_4$ samples.

Published on 08 February 2021. Downloaded by NANJING UNIVERSITY on 3/21/2021 12:48:35 PM.

### 3.3. Photoelectrochemical and $CO_2$ adsorption/activation properties

The PL spectra and photocurrents were used to investigate the photo-induced electron–hole pair separation efficiency. As observed in Fig. 3a, all the samples showed a broad PL peak centered at 450 nm. Compared with CeCN and CeCN-$H_2$, the PL emission intensity of CeCN-$N_2$ significantly decreased, suggesting that a higher electron–hole separation efficiency was present on CeCN-$N_2$, while the photo-generated charges were easily facilitated to be recombined on the CeCN and CeCN-$H_2$ samples. Besides, the transient photocurrent responses were determined for 0.5 h under light illumination to investigate the charge separation and the last seven cycles are shown in Fig. 3b. Generally, a higher photocurrent intensity suggests more efficient transfer of the photo-generated charges. The photocurrent response intensities followed the order CeCN-$N_2$ > CeCN > CeCN-$H_2$, further confirming that a more efficient photoinduced electron transfer occurs on the CeCN-$N_2$ catalyst, whereas, compared with CeCN, the $H_2$-pretreated CeCN-$H_2$ catalyst had less available photoinduced electrons, which is consistent with the reaction activity order. The EIS responses also indicate that more effective separation of photo-generated electron–hole pairs and faster interfacial charge-transfer occurred in the CeCN-$N_2$ samples according to the smallest arc radius on the EIS Nyquist plot shown in Fig. 3c.

In addition, it is well-known that reactant adsorption on the catalyst surface is of great importance to photocatalysis; therefore, $CO_2$-TPD characterization was used to investigate the interaction of the $CO_2$ reactant on different g-$C_3N_4$/$CeO_2$ catalysts in comparison. The $CO_2$-TPD results are shown in Fig. 4a. The peaks centered at *ca.* 150 (molecularly adsorbed $CO_2$), 350 ($HCO_3^-$ or $HCO_2^-$), and 450 °C (bidentate carbonates) are attributed to e, medium, and strong basic sites of the catalysts, respectively. The obvious desorption peaks at above 500 °C in the TPD-$CO_2$ curves were assigned

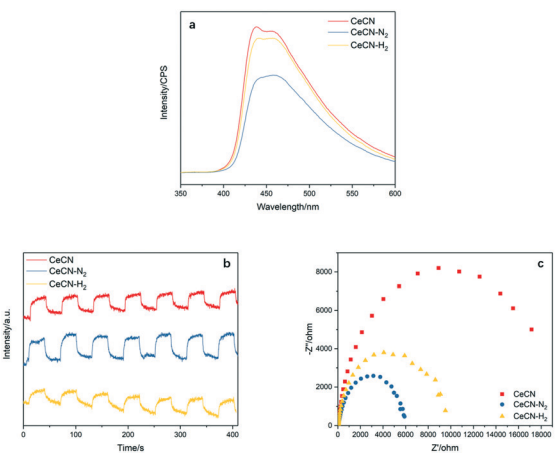


Fig. 3 (a) PL spectra, (b) transient photocurrent response, and (c) EIS spectra of the $CeO_2$/g-$C_3N_4$ samples.

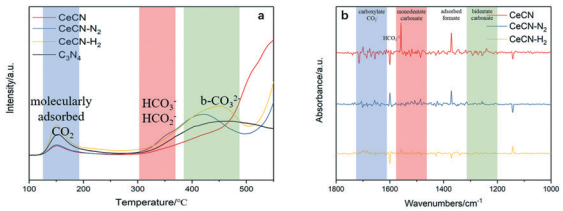


Fig. 4 (a) $CO_2$-TPD and (b) *in situ* $CO_2$ adsorption DRIFTS under the light illumination of the $CeO_2$/g-$C_3N_4$ samples.

to the decomposition of g-$C_3N_4$. The $CO_2$ adsorption amount was increased after $CeO_2$ loading in comparison to that on pure g-$C_3N_4$. Furthermore, the peak area at 350 °C is more obvious on the CeCN-$N_2$ sample than on the other two samples, suggesting that CeCN-$N_2$ was provided with more number of medium chemisorption species. Generally, the medium base site plays a significant role in the adsorption and activation of $CO_2$ in photo-reduction. On this basis, $CO_2$ molecules were more beneficial for the adsorption and activation on CeCN-$N_2$, leading to better performance of $CO_2$ photoreduction. On the other hand, stronger base sites were observed on the CeCN-$H_2$ sample, which were not helpful for $CO_2$ activation, and thus, poorer activity was obtained on CeCN-$H_2$.

In order to further confirm the different abilities of $CO_2$ adsorption and activation on the g-$C_3N_4$/$CeO_2$ catalysts, the *in situ* DRIFTS of the $CeO_2$/g-$C_3N_4$ samples under light illumination were obtained by the deduction of the background spectra for the saturated adsorption of $CO_2$ in dark to determine the formed reaction intermediate during the photocatalytic $CO_2$ reduction. The corresponding results are displayed in Fig. 4b. The $CO_2$ adsorption peaks could visually reveal the generation and disappearance information of the surface species once light illumination occurs, *i.e.*, the positive peaks showed that some species were generated after illumination, while the negative peaks were attributed to the species reacted or desorbed. According to the literature, the observed vibrational bands at 1680 and 1376 $cm^{-1}$ were assigned to carboxylate $CO_2^-$ and the adsorbed formate species, besides $HCO_3^-$ (1600 $cm^{-1}$), monodentate carbonate (1580 $cm^{-1}$), and bidentate carbonate (1260 $cm^{-1}$).[27,30,31] After illumination, more $HCO_3^-$ and carboxylate $CO_2^-$ species were formed on CeCN-$N_2$, while the $HCO_3^-$ species on CeCN decreased and more carbonate species were generated. It has been reported that the generation of carboxylate species and $HCO_3^-$ indicated that $CO_2$ reactant was easier to be activated.[32] In addition, few reaction intermediates were formed on CeCN-$H_2$, probably because of the high recombination of the photoelectrons and the holes.

On the basis of the PL, photocurrent, $CO_2$-TPD, and *in situ* DRIFTS results, it was proposed that $N_2$-pretreated $CeO_2$/g-$C_3N_4$ provided more available photo-generated charges, medium base sites, and reaction intermediate species in the photoreduction process, which synergistically improved the photocatalytic performance of $CO_2$ reduction. On the other hand, for the $H_2$-pretreated $CeO_2$/g-$C_3N_4$, less efficient photo-


This journal is © The Royal Society of Chemistry 2021

Published on 08 February 2021. Downloaded by NANJING UNIVERSITY on 3/21/2021 12:48:35 PM.

electrons, stronger base site, and few carbonate species were present, and thus, the poorest activity was obtained. Why did different pretreatment atmospheres have various influences on the photo-induced electron–hole separation efficiency and the $CO_2$ adsorption/activation abilities of the $CeO_2$/g-$C_3N_4$ photocatalysts? In particular Especially, the reason for the opposite results on CeCN-$N_2$ and CeCN-$H_2$ were still not clear. Therefore, the mechanisms of interfacial interactions of the $CeO_2$/g-$C_3N_4$ photocatalysts with different pretreatment atmospheres were investigated.

### 3.4. Mechanism of interfacial interactions

In order to gain further insight into the interfacial electronic structures, FT-IR and XPS characterizations were carried out as follows. As shown in Fig. 5a, the characteristic vibrational peaks attributed to g-$C_3N_4$ could be observed in all the samples. The peak at 820 $cm^{-1}$ was attributed to the bending vibration of the heptazine rings on g-$C_3N_4$ and the peaks ranging from 1100 to 1800 $cm^{-1}$ were assigned to the typical stretching modes of the heterocycles.[33] It was found that compared with CeCN-$N_2$ and CeCN, the peaks of the CeCN-$H_2$ photocatalyst were slightly blue-shifted. According to the literature,[34] the peak shift in the spectrum of CeCN-$H_2$ was attributed to the fact that the electrons were introduced to g-$C_3N_4$ and the conjugation network structure was slightly strengthened. On this basis, it was deduced that on the CeCN-$H_2$ interface, g-$C_3N_4$ with negative charge and $CeO_2$ with positive charge led to the formation of a built-in electronic field.

Moreover, the XPS spectra of C 1s and N 1s are displayed in Fig. 5b and c, respectively, in order to explore the above interfacial electronic effects. In the C 1s spectra, the peak at 288.2 eV was assigned to the $sp^2$-bonded carbon atom (N–C═N) in the aromatic rings of g-$C_3N_4$. Besides, the N 1s spectra could be fitted into the four peaks, as shown in Fig. 5c. The peaks at about 398.6, 399.3, 400.8, and 404.2 eV corresponded to the $sp^2$ hybridized aromatic N atom bonded to C atoms (C═N–C), tertiary nitrogen (H–N–$C_2$ or N–$C_3$), amino functional group, and charging effect localization in the heterocycle, respectively.[35] Compared to the CeCN composite, the binding energies of the N 1s and C 1s peaks shifted to higher values on CeCN-$N_2$, while the peaks of CeCN-$H_2$ shifted to lower values, suggesting that the electron densities of CN were decreased on CeCN-$N_2$ and increased on CeCN-$H_2$, respectively. On this basis, the electrons migrated from g-$C_3N_4$ to $CeO_2$ on the CeCN-$N_2$ interface, leading to g-$C_3N_4$ and $CeO_2$ with positive and negative charges, respectively. On the other hand, the transfer direction on CeCN-$H_2$ was opposite, *i.e.*, the electrons migrated from $CeO_2$ to g-$C_3N_4$ on the CeCN-$H_2$ interface, which is in agreement with the FT-IR results.

In order to accurately describe the electron transfer progress on the $CeO_2$ and g-$C_3N_4$ interface, the band structures were calculated *via* UV-vis diffuse reflectance spectroscopy and the Mott–Schottky plots. The band gap values (Eg) of the samples were determined by the tangent lines of the $(ahv)^{1/2}$ against energy ($hv$) plot, as shown in Fig. S3a and b† and the flat band potentials ($E_{fb}$) were determined by the tangent lines of the M–S curves in Fig. S3c and d.† The potentials *versus* standard hydrogen electrode (SHE) were calculated based on eqn (1).

$$E(vs.\ \mathrm{SHE}) = E(vs.\ \mathrm{Ag/AgCl}) + 0.0591 \times \mathrm{pH} + 0.2224. \quad (1)$$

Also, it is known that the conduction band potentials ($E_{CB}$) for an n-type semiconductor is more negative by about −0.1 or −0.2 V than its flat band potential.[36] Above all, the band gap values, the conduction potentials, and the calculated valence band potentials ($E_{VB}$) are listed as Table S1† and the band gap structures are shown in Fig. 6. For CeCN-$N_2$, the photoinduced electrons were more likely to concentrate towards g-$C_3N_4$ on account of the built-in electronic filed (*i.e.*, positively charged g-$C_3N_4$) at the interface, leading to the formation of a g-$C_3N_4$/$CeO_2$ Z-scheme photocatalytic system with a stronger reduction potential. In contrast, for CeCN-$H_2$, the photoinduced electrons transferred to $CeO_2$ and tended to recombine with the holes, leading to increased photo-generated charge recombination. In addition, the Z-scheme CeCN-$N_2$ photocatalytic system was provided with more

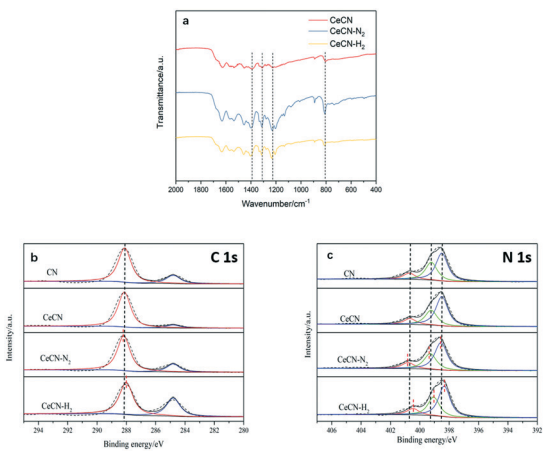


Fig. 5 (a) FT-IR spectra, (b) C 1s and (c) N 1s XPS spectra of the $CeO_2$/g-$C_3N_4$ samples.

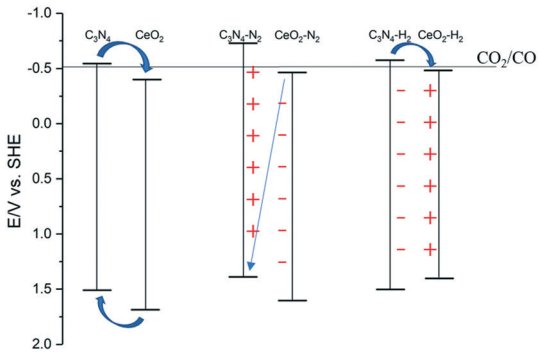


Fig. 6 The band gap structures of the $CeO_2$/g-$C_3N_4$ samples.

Published on 08 February 2021. Downloaded by NANJING UNIVERSITY on 3/21/2021 12:48:35 PM.

negative reduction CB potential of g-$C_3N_4$ and not the CB of $CeO_2$; thus, Z-scheme CeCN-$N_2$ facilitated the CO production more than that by type II (CeCN), according to the standard redox potential of $CO_2$/CO (−0.52 V).

Furthermore, we tried to use a radical trap to further prove the formation of the Z-scheme. Benzoquinone (BQ) was applied to scavenge the $^{\bullet}O_2^-$ radicals in the methylene blue (MB) solution compared to that with no scavengers. The activities of MB degradation are shown in Fig. S4.† The standard redox potential of $O_2/^{\bullet}O_2^-$ is −0.33 eV, which was below the conductive band of both $CeO_2$ and g-$C_3N_4$; thus, the degradation efficiency of MB decreased as BQ was added for the CeCN-$N_2$ and CeCN-$H_2$ catalysts. However, the activity of CeCN-$N_2$ degraded more than that of CeCN-$H_2$, revealing that more $^{\bullet}O_2^-$ radicals were presented on CeCN-$N_2$. Therefore, combining the above results, it could be suggested that the Z-scheme system was formed only in CeCN-$N_2$.

To further explore the basis of different band gap structures, XPS and EPR were employed to study the oxygen defects of CeCN, CeCN-$N_2$, and CeCN-$H_2$ and the results were compared. The XPS spectra of O 1s is shown in Fig. 7a. The O 1s spectrum consist of three peaks at binding energy of 529.6 eV, 531.9 eV, and 533.0 eV, which can be attributed to the lattice oxygen ($O_L$), the chemisorbed oxygen or/and weakly bonded oxygen species ($O_C$), and the surface oxygen by the hydroxyl species and/or adsorbed water species on the surface ($O_S$), respectively.[24,37] CeCN-$N_2$ and CeCN-$H_2$ showed lesser $O_L/O_{(s+c)}$ ratio than the CeCN photocatalysts, indicating the higher relative concentration of the oxygen defects. It was also found that the position of lattice oxygen on CeCN-$N_2$ and CeCN-$H_2$ shifted to higher binding energy than that of CeCN, which suggested that the electronic density of the lattice oxygen decreased, possibly resulting from the formation of oxygen defects on the CuCN-$N_2$ and CeCN-$H_2$ samples.

The EPR results shown in Fig. 7b further confirmed the above. The signal of $g$ = 1.956 was recognized as $Ce^{3+}$ and the signal of $g$ = 2.008 was attributed to an unpaired electron trapped on an oxygen vacancy site.[38,39] It was found that the signal intensity of the oxygen vacancy was the most obvious on the CeCN-$H_2$ sample, followed by CeCN-$N_2$, and CeCN had the weakest intensity. Based on the above characterizations, the order of the relative concentration of oxygen defects were as follows: CeCN-$H_2$ > CeCN-$N_2$ > CeCN. The up-shifted $E_{VB}$ of $CeO_2$ could contribute to the enhanced relative concentration of the oxygen defects on $CeO_2$. Besides,

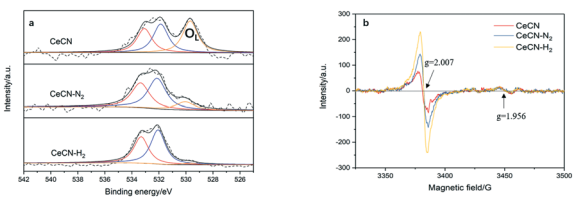


Fig. 7 (a) O 1s XPS spectra and (b) EPR results of the $CeO_2$/g-$C_3N_4$ samples.

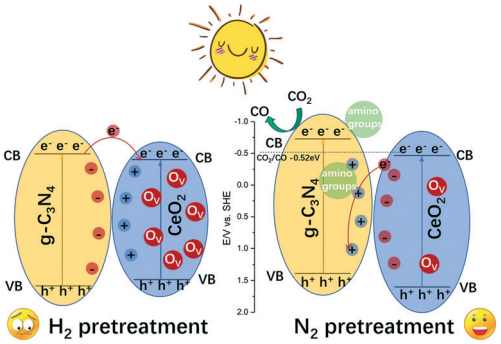


Fig. 8 The possible reaction mechanism of $CO_2$ photoreduction on the $CeO_2$/g-$C_3N_4$ samples.

the FT-IR spectra of g-$C_3N_4$ under different atmosphere treatment are shown in Fig. S5.† The broad absorption band at 3100–3300 $cm^{-1}$ is associated with the stretching mode of the primary and secondary amines as well as their intermolecular hydrogen bonding interactions. The peak intensities of the peaks at 3160 $cm^{-1}$ ($I_1$) and 1628 $cm^{-1}$ ($I_2$) are listed in Table S2† and the relative peak intensity at 3100–3300 $cm^{-1}$ ($I_1/I_2$) of CN-$N_2$ is higher than that of CN and CN-$H_2$, which is in the order CN-$N_2$ (0.44) > CN-$H_2$ (0.40) > CN (0.38) and is attributed to more amino groups on CN-$N_2$. Thus, nitrogen-treated g-$C_3N_4$ could introduce more amino groups in the heterocycles, and the higher valence band potential of CN-$N_2$ and the stronger reduction ability of CeCN-$N_2$ were present.[40]

In short, the schematic illustration is shown in Fig. 8. Compared to $N_2$, $H_2$ with stronger reduction ability made CeCN-$H_2$ have more oxygen defects on $CeO_2$; thus, $CeO_2$ possessed positive charges. On the other hand, in the process of $N_2$ pretreatment, the generated amino groups in the heterocycles of g-$C_3N_4$ were involved in the formation of ammonium, and thus, g-$C_3N_4$ had positive charges on CeCN-$N_2$. Due to the above treatment atmosphere inducing built-in electronic fields, the Z-scheme photocatalytic system with stronger reduction potential was formed on CeCN-$N_2$, leading to the best activity. In contrast, for CeCN-$H_2$, the photoinduced electrons transferred to $CeO_2$ and tended to recombine with the holes, thus giving the poorest activity.

## Conclusions

$CeO_2$/g-$C_3N_4$ catalysts were treated with different atmospheres and the effects were compared. $N_2$ pretreatment generated amino groups with positive charges on the g-$C_3N_4$ of CeCN-$N_2$, and the formed built-in electronic field led to the formation of the Z-scheme photocatalytic system with stronger reduction potential, faster charge transfer, and medium basic sites, which synergistically improved the activity of $CO_2$ photoreduction. On the other hand, $H_2$ pretreatment provided CeCN-$H_2$ with too many oxygen defects on $CeO_2$ with positive charges, the photoinduced electrons transferred to $CeO_2$ and tended to recombine with the holes,


This journal is © The Royal Society of Chemistry 2021

Published on 08 February 2021. Downloaded by NANJING UNIVERSITY on 3/21/2021 12:48:35 PM.

thus giving the poorest activity. This work could provide a basic guideline for designing efficient Z-scheme catalysts.

## Conflicts of interest

There are no conflicts to declare.

## Acknowledgements

The authors gratefully acknowledge the financial support from the National Natural Science Foundation of China (21707066, and 21908092).

## References

1 *IEA Finds $CO_2$ Emissions Flat for Third Straight Year Even as Global Economy Grew in 2016*, https://www.iea.org/newsroom/news/2017/march/iea-finds-co2-emissions-flat-for-third-straight-year-even-as-global-economy-grew.html.
2 *Forecast of Worldwide Carbon Dioxide Emissions through 2040*, https://www.statista.com/statistics/263980/forecast-of-global-carbon-dioxide-emissions/.
3 H. Yamashita, K. Mori, Y. Kuwahara, T. Kamegawa, M. Wen, P. Verma and M. Che, *Chem. Soc. Rev.*, 2018, **47**, 8072–8096.
4 S. Chu and A. Majumdar, *Nature*, 2012, **488**, 294–303.
5 K. Mori, K. Miyawaki and H. Yamashita, *ACS Catal.*, 2016, **6**, 3128–3135.
6 M. Zhang, W. Jiang, D. Liu, J. Wang, Y. Liu, Y. Zhu and Y. Zhu, *Appl. Catal., B*, 2016, **183**, 263–268.
7 R. Kuriki, O. Ishitani and K. Maeda, *ACS Appl. Mater. Interfaces*, 2016, **8**, 6011–6018.
8 J. Qin, J. Huo, P. Zhang, J. Zeng, T. Wang and H. Zeng, *Nanoscale*, 2016, **8**, 2249–2259.
9 Y. Luo, J. Wang, S. Yu, Y. Cao, K. Ma, Y. Pu, W. Zou, C. Tang, F. Gao and L. Dong, *J. Mater. Res.*, 2018, **33**, 1268.
10 T. Y. Ma, J. Ran, S. Dai, M. Jaroniec and S. Z. Qiao, *Angew. Chem.*, 2015, **127**, 4729–4733.
11 X. She, J. Wu, H. Xu, J. Zhong, Y. Wang, Y. Song, K. Nie, Y. Liu, Y. Yang and M. T. F. Rodrigues, *Adv. Energy Mater.*, 2017, **7**, 1700025.
12 G. Zhang, Z.-A. Lan, L. Lin, S. Lin and X. Wang, *Chem. Sci.*, 2016, **7**, 3062–3066.
13 H. Wang, Q. Li, S. Zhang, Z. Chen, W. Wang, G. Zhao, L. Zhuang, B. Hu and X. Wang, *Catal. Today*, 2019, **335**, 110–116.
14 J. Xu, M. Fujitsuka, S. Kim, Z. Wang and T. Majima, *Appl. Catal., B*, 2019, **241**, 141–148.
15 J. Liao, W. Cui, J. Li, J. Sheng, H. Wang, P. Chen, G. Jiang, Z. Wang and F. Dong, *Chem. Eng. J.*, 2020, **379**, 122282.
16 J. Kong, G. Li, M. Wen, J. Chen, H. Liu and T. An, *J. Catal.*, 2019, **370**, 88–96.
17 L. Xu and J. Wang, *Environ. Sci. Technol.*, 2012, **46**, 10145–10153.
18 X. Yao, Y. Xiong, W. Zou, L. Zhang, S. Wu, X. Dong, F. Gao, Y. Deng, C. Tang and Z. Chen, *Appl. Catal., B*, 2014, **144**, 152–165.
19 C. Yang, Q. Li, Y. Xia, K. Lv and M. Li, *Appl. Surf. Sci.*, 2019, **464**, 388–395.
20 L. Chen, D. Meng, X. Wu, A. Wang, J. Wang, Y. Wang and M. Yu, *J. Phys. Chem. C*, 2016, **120**, 18548–18559.
21 M. Liang, T. Borjigin, Y. Zhang, B. Liu, H. Liu and H. Guo, *Appl. Catal., B*, 2019, **243**, 566–575.
22 X. Liu, L. He, X. Chen, L. Du, X. Gu, S. Wang, M. Fu, F. Dong and H. Huang, *Int. J. Hydrogen Energy*, 2019, **44**, 16154–16163.
23 C. Zhu, Y. Wang, Z. Jiang, F. Xu, Q. Xian, C. Sun, Q. Tong, W. Zou, X. Duan and S. Wang, *Appl. Catal., B*, 2019, **259**, 118072.
24 H. Hu, J. Hu, X. Wang, J. Gan, M. Su, W. Ye, W. Zhang, X. Ma and H. Wang, *Catal. Sci. Technol.*, 2020, **10**, 4712–4725.
25 G. B. Della Mea, L. P. Matte, A. S. Thill, F. O. Lobato, E. V. Benvenutti, L. T. Arenas, A. Jürgensen, R. Hergenröder, F. Poletto and F. Bernardi, *Appl. Surf. Sci.*, 2017, **422**, 1102–1112.
26 S. Peng, X. Sun, L. Sun, M. Zhang, Y. Zheng, H. Su and C. Qi, *Catal. Lett.*, 2019, **149**, 465–472.
27 Y. Pu, Y. Luo, X. Wei, J. Sun, L. Li, W. Zou and L. Dong, *Appl. Catal., B*, 2019, **254**, 580–586.
28 X. Yang, Z. Chen, J. Xu, H. Tang, K. Chen and Y. Jiang, *ACS Appl. Mater. Interfaces*, 2015, **7**, 15285–15293.
29 W. Chen, Y.-X. Hua, Y. Wang, T. Huang, T.-Y. Liu and X.-H. Liu, *J. Catal.*, 2017, **349**, 8–18.
30 Y. Yu, Y. M. Chan, Z. Bian, F. Song, J. Wang, Q. Zhong and S. Kawi, *Int. J. Hydrogen Energy*, 2018, **43**, 15191–15204.
31 C. Zhu, X. Wei, W. Li, Y. Pu, J. Sun, K. Tang, H. Wan, C. Ge, W. Zou and L. Dong, *ACS Sustainable Chem. Eng.*, 2020, **8**, 14397–14406.
32 L. Liu, Y. Jiang, H. Zhao, J. Chen, J. Cheng, K. Yang and Y. Li, *ACS Catal.*, 2016, **6**, 1097–1108.
33 S. Hu, L. Ma, J. You, F. Li, Z. Fan, G. Lu, D. Liu and J. Gui, *Appl. Surf. Sci.*, 2014, **311**, 164–171.
34 Y. Wang, W. Yang, X. Chen, J. Wang and Y. Zhu, *Appl. Catal., B*, 2018, **220**, 337–347.
35 D. Gao, Q. Xu, J. Zhang, Z. Yang, M. Si, Z. Yan and D. Xue, *Nanoscale*, 2014, **6**, 2577–2581.
36 X. Hao, J. Zhou, Z. Cui, Y. Wang, Y. Wang and Z. Zou, *Appl. Catal., B*, 2018, **229**, 41–51.
37 Y. Wang, F. Wang, Y. Chen, D. Zhang, B. Li, S. Kang, X. Li and L. Cui, *Appl. Catal., B*, 2014, **147**, 602–609.
38 H. Kaftelen, K. Ocakoglu, R. Thomann, S. Tu, S. Weber and E. Erdem, *Phys. Rev. B: Condens. Matter Mater. Phys.*, 2012, **86**, 014113.
39 K. Zhao, J. Qi, H. Yin, Z. Wang, S. Zhao, X. Ma, J. Wan, L. Chang, Y. Gao and R. Yu, *J. Mater. Chem. A*, 2015, **3**, 20465–20470.
40 D. Zhang, G. Tan, M. Wang, B. Li, M. Dang, H. Ren and A. Xia, *Mater. Res. Bull.*, 2020, **122**, 110685.